Pacific Meridional Mode Implicated as a Prime Driver of Decadal Summer Temperature Variation over Taiwan

CHIEH-TING TSAI,[a,b] YI-CHI WANG,[a] WAN-LING TSENG,[a,c] AND LI-CHIANG CHIANG[a]

[a] *Research Center for Environmental Changes, Academia Sinica, Taipei, Taiwan*
[b] *International Degree Program in Climate Change and Sustainable Development, National Taiwan University, Taipei, Taiwan*
[c] *Ocean Center, National Taiwan University, Taipei, Taiwan*

(Manuscript received 9 December 2023, in final form 17 December 2024, accepted 22 January 2025)

ABSTRACT: The Pacific meridional mode (PMM) is a climate phenomenon in the eastern Pacific, characterized by strong wind–sea surface temperature (SST) interactions. During its positive phase, an atypical north–south SST gradient develops in the northeastern subtropical Pacific, leading to significant global teleconnections, which refer to the mutual influence or correlation between atmospheric or oceanic changes in two distant regions of Earth. This study examines the relationship between historical summer temperature data for Taiwan (June–August) and PMM indices over a 59-yr period (1960–2018), revealing a significant correlation between the two. Regressed large-scale circulations indicate the eastward propagation of a wave train across the northern Pacific into East Asia, inducing anticyclonic circulations near southeastern China and Taiwan, accompanied by subsidence, which refers to the vertical downward movement of air masses in the atmosphere, typically associated with high pressure systems and dry weather conditions, that stabilize the atmosphere. This stabilization reduces the influence of seasonal southwesterly winds while increasing shortwave radiation at the surface, thereby raising surface temperatures in Taiwan. Our findings are further supported by linear baroclinic model (LBM) experiments featuring PMM-like heating forcing and by large-scale responses to PMM-related SST patterns simulated in CMIP6 historical runs. While these results suggest that the PMM could be a valuable tool for predicting Taiwan's summer climate on decadal time scales, we also observe model uncertainties in simulating the teleconnection patterns of PMM-related SSTs in East Asia, including Taiwan's summer temperature response. These findings underscore the need for further investigation into the complex interplay between PMM circulation responses, seasonal monsoons, and other components of climate systems simulated in climate models.

KEYWORDS: Atmospheric circulation; Teleconnections; Summer/warm season; Heat budgets/fluxes; Climate variability; Decadal variability

1. Introduction

In recent decades, there has been a growing demand for climate information on time scales ranging from subseasonal to decadal, driven by the pursuit of seamless climate prediction (Hoskins 2013; Ruti et al. 2020). Among these time scales, climate information spanning 5–10 years is of paramount importance for the planning of energy resources, agriculture, water management, and disaster preparedness (Dunstone et al. 2022). It empowers stakeholders to formulate medium- to long-term adaptation strategies and develop appropriate infrastructure (Goddard 2016; Trenberth et al. 2016). However, compared to the predictability of interannual phenomena and projections for the end of the century, decadal-scale climate prediction, especially its regional impacts, remains a challenging endeavor (Gao et al. 2018). Therefore, it is essential to explore the dominant mechanisms influencing regional climate variations on a decadal time scale to advance our capacity for regional impact prediction.

In this study, we focus on the summer temperature of Taiwan, a region situated in the subtropical northwestern Pacific, nestled between the Asian continent and the Pacific Ocean. Taiwan's unique geographical location results in complex climate variations influenced by both tropical and midlatitude climate systems. Previous research has examined the role of nearby Pacific variability in modulating summer temperatures in Taiwan. For instance, Lo and Hsu (2008) highlighted a regime shift around the 1950s characterized by the phase transition of the Pacific decadal oscillation (PDO). On an interannual time scale, El Niño–Southern Oscillation (ENSO) has been linked to the induction of summer heatwaves (Wu et al. 2020). As part of the interannual variability of the summer Asian monsoon, the Pacific–Japan pattern has been found to modulate summer temperatures and variations in hot extremes in Taiwan (Tseng et al. 2023). Additionally, studies have shown that cold sea surface temperatures (SSTs) over the Indian Ocean and tropical Pacific can induce anomalous warm advection, leading to autumn temperature increases over Taiwan through the generation of a low-level Rossby wave–like circulation anomaly (Chen et al. 2008). However, none of these studies have provided a comprehensive explanation for the major variations in Taiwan's summer temperatures on a decadal time scale, suggesting that the primary modulating mechanism remains unclear.

An increasing body of research has emphasized the significant role played by the Pacific meridional mode (PMM) in shaping climate patterns in the western Pacific. PMM stands

Denotes content that is immediately available upon publication as open access.

Supplemental information related to this paper is available at the Journals Online website: https://doi.org/10.1175/JCLI-D-23-0734.s1.

Corresponding author: Wan-Ling Tseng, wtseng@ntu.edu.tw

DOI: 10.1175/JCLI-D-23-0734.1

out as one of the dominant Pacific decadal modes, situated in the eastern Pacific, characterized by a strong wind–SST coupling spanning approximately 10°–30°N and 160°E–160°W (Chiang and Vimont 2004). PMM often precedes ENSO events, with signals of anomalous SST warming appearing as early as May–June. Notably, the PMM-related SST signature in the subtropical Pacific is often considered a precursor to ENSO events (Yu 2015). Additionally, the PMM has shifted from interannual variations to experiencing interdecadal enhancement (≥8 yr). This intensification began in the early 1990s, driven by a phase change in the Atlantic multidecadal oscillation (AMO), which led to a stronger subtropical Pacific high. Furthermore, the increasing positive correlation between the North Atlantic tripole (NAT) and the PMM may also be contributing to the PMM's growing impact on the western North Pacific (Kao et al. 2022).

PMM exerts strong impacts on the western Pacific region, including tropical cyclones, rainfall, and extreme heat. For instance, it is linked to the eastward shift in tropical cyclone genesis, as observed in the summer of 2015 (Hong et al. 2018). Studies have confirmed a positive correlation between PMM frequency and the occurrence of intense typhoons during peak typhoon season (Song et al. 2023; C. Wang et al. 2023), attributed to Matsuno–Gill-type Rossby wave responses, which reduce vertical wind shear and increase low-level vorticity, favoring intense cyclones (Gao et al. 2018). PMM also influences decadal rainfall variations in Taiwan, driving extreme dryness from October to December through induced anomalous anticyclones over the South China Sea (Hung and Shih 2019). On the other hand, Kao et al. (2018) indicate that since the 1980s, the PMM-like SST has strengthened, inducing an east–west circulation and subsidence motion in the western North Pacific (WNP), enhancing the southwesterly flow, and increasing spring rainfall in Taiwan. The differing results in each study show that the relationship between rainfall in Taiwan and PMM remains debated. Beyond cyclones and rainfall, PMM is linked to increased intensity and frequency of extreme heat and reduced rainfall in eastern China, due to interactions with the East Asian jet stream and midlatitude Rossby waves, leading to subsidence over East Asia (Luo et al. 2020).

However, to date, no study has quantified the influence of PMM on Taiwan's summer climate and elucidated the underlying physical mechanisms using modeling approaches. Given the increasing significance of rising summer temperatures and the frequent occurrence of heatwaves for public health and energy planning, this study aims to establish the modulation of the PMM on summer temperatures in Taiwan on a decadal time scale through regression analysis and climate modeling experiments. By combining 59 years of local observational data and global reanalysis data (1960–2018), we demonstrate that the PMM likely serves as a dominant factor influencing major summer temperatures in Taiwan on a decadal scale. Additionally, our climate modeling experiments confirm that PMM-related warm SST anomalies over the eastern Pacific can force observed anticyclonic anomalies and subsidence over East Asia and Taiwan through a cross-Pacific circulation pattern, resulting in unusually hot summers in Taiwan. The remainder of this paper is organized as follows: Section 2 outlines the data, model, and methodology employed. Section 3 presents the analytical results. Section 4 discusses the response of the large-scale Pacific circulation to PMM-like SST anomalies (SSTAs) using the Taiwan Earth System Model, version 1, and how these responses are represented in the historical simulations of phase 6 of the Coupled Model Intercomparison Project (CMIP6). Finally, we provide a discussion and summary in section 5.

2. Datasets and methodology

a. Datasets

1) Local temperature dataset of Taiwan

The temperature data for summer in Taiwan in this study are obtained from the Taiwan Climate Change Projection Information and Adaptation Knowledge Platform (TCCIP; https://tccip.ncdr.nat.gov.tw/; Yang et al. 2024), which is funded by the National Science and Technology Council of Taiwan. The monthly observation data are provided in a gridded format with a spatial resolution of 5 km, spanning the time from 1960 to 2018. This dataset has been utilized in numerous peer-reviewed studies investigating climate impacts over Taiwan. It incorporates data from various sources such as weather stations and agriculture stations (Huang and Chang 2018; Henny et al. 2021, 2023; Tseng et al. 2023). It should be noted that regions with lower station density (e.g., mountain areas) have higher data uncertainty and larger estimation errors (Yang et al. 2024). Therefore, this study focuses on areas below an elevation of 1000 m as the research area. Using population data from the Department of Household Registration, Ministry of the Interior, Taiwan, we found the areas below 1000 m in Taiwan cover more than 99.5% of the population distribution, representing the main residential areas in Taiwan (not shown; Department of Household Registration, Ministry of the Interior, Taiwan; https://www.ris.gov.tw). By focusing on areas below 1000 m, this study focuses on the climate impacts on densely populated regions, which has more implications on further climate information needed for climate adaptation of Taiwan's society.

2) Global SST and reanalysis dataset

The SST data are based on the monthly version of the Hadley Centre Sea Ice and SST dataset (HadISST) from the Met Office Hadley Centre (Rayner et al. 2003). The rest of the atmospheric variables utilize the fifth major global reanalysis produced by the European Centre for Medium-Range Weather Forecasts (ERA5; Hersbach et al. 2020). The data are based on the Integrated Forecast System model cycle 41r2 with a native model resolution of T1279L137 with data assimilation of satellites, in situ observations, and soundings. The data used here include sea level pressure (SLP), horizontal and vertical winds, and surface radiation and heat fluxes.

3) CMIP6 HISTORICAL RUNS

The response of large-scale Pacific circulation to the PMM-related SST pattern is analyzed using the historical runs in the CMIP6, which are downloaded from Earth System Grid Federation CMIP6 archive (https://esgf-node.llnl.gov/search/cmip6/). We employ r1i1p1f1 simulations and selected models with a resolution exceeding 2.5° × 2.5° that encompassed wind fields (zonal wind, meridional wind, and vertical velocity in pressure coordinates), temperatures (near-surface air temperature and air temperature), geopotential height, and sea level pressure. A total of 37 models that met the aforementioned criteria were selected for analysis (Table S1 in the online supplemental material).

b. Methodology

1) INDEX FOR IDENTIFYING PMM

This study used the monthly PMM indices calculated from the NOAA Earth System Research Laboratory (ESRL; https://www.esrl.noaa.gov/psd/data/timeseries/monthly/PMM/, accessed in 2022). The PMM is identified as the first coupled mode through maximum covariance analysis (MCA) of SST and 10-m wind fields over the tropical and subtropical Pacific region (21°S–32°N, 74°W–15°E), following the method introduced by Chiang and Vimont (2004). To isolate the PMM signal from other climate influences, preprocessing steps were applied to the original SST and wind fields, including spatial smoothing, removal of the seasonal cycle, linear trend, and application of a 3-month running mean. The Pacific cold tongue index, which represents the ENSO signal, was also removed before conducting the MCA analysis. For this study, we used the monthly average PMM indices for June–August (JJA) from 1960 to 2018. Additionally, a 5-yr moving average was applied to the PMM indices to further minimize the influence of ENSO signals, which can also affect Taiwan's climate.

On the other hand, the PMM signals simulated in CMIP6 models are determined by extracting the most variation mode with the SST data over the east Pacific region (21°S–32°N and 74°W–15°E) with empirical orthogonal function (EOF) analysis. Unlike the wind–SST PMM index provided by NOAA ESRL, we simplify the calculation by using only SST data in EOF analysis to identify the PMM pattern (Richter et al. 2022). After several preprocessing steps including removal of seasonal averages, linear trend, and cold tongue index (CTI) signals, the first mode of EOF (EOF1) analysis is defined as the PMM pattern, with the first principal component (PC1) serving as the PMM index. The sensitivity test we conducted shows that the SST-based PMM index has a robust characterization of PMM as the SST–wind-based PMM index with a correlation coefficient of 0.86 (not shown). We have found that more than 80% of CMIP6 models can capture the observed PMM pattern with the EOF1 mode with a correlation coefficient exceeding 0.3 (not shown). This study utilizes the complete TCCIP observational dataset from 1960 to 2018 to capture decadal variations in Taiwan's summer temperatures. Using this long data series provides more robust signals of decadal variation. However, analyses of shorter periods, such as 1980–2020, show lower correlation coefficients between the PMM index and Taiwan's summer temperatures, despite a similar response pattern. Further investigation is needed to understand the factors driving these changes in the PMM–Taiwan relationship during more recent decades.

2) THERMODYNAMIC BUDGET ANALYSIS

To investigate the physical processes contributing to temperature changes, we conducted a thermodynamic budget analysis at the near-surface level of 925 hPa over the focal region of Taiwan. The thermodynamic budget analysis quantifies the balance of heat sources and sinks within the atmosphere, enabling the study of energy changes and their distribution. This approach helps to identify the mechanisms driving temperature variations. The budget equation, originally proposed by Yanai et al. (1973), is expressed as follows:

$$\left(\frac{P}{P_0}\right)^{\kappa}\left(\frac{\partial\theta}{\partial t}+\upsilon\nabla\theta+\omega\frac{\partial\theta}{\partial p}\right)=\frac{Q_1}{C_P},$$

where P represents the pressure and P_0 represents the reference pressure at 1000 hPa. The term $\kappa = R/C_p$ is the adiabatic index, defined as the ratio of the specific heat at constant pressure to the specific heat at constant volume for a gas. The term $\partial\theta/\partial t$ represents the rate of change of temperature θ with respect to time t. The term υ represents the advective wind term, and $\nabla\theta$ signifies the advective term's contribution to temperature change. The term $\omega(\partial\theta/\partial p)$ represents the vertical term's adiabatic heating. The term Q_1 represents the residual heating term, which represents the contribution from physical processes, including radiation cooling/heating, convection-related heating, and planetary boundary layer processes. The term C_p is the diabatic heating rate normalized by the specific heat at constant pressure.

To emphasize the impact of different physical processes on $\partial\theta/\partial t$, we present the equation in the following manner:

$$\frac{\partial\theta}{\partial t}=\frac{Q_1}{C_P}-p^*U\frac{\partial\theta}{\partial x}-p^*V\frac{\partial\theta}{\partial y}-p^*\omega\frac{\partial\theta}{\partial p},$$

where $p^* = [(P/P_0)^k]^{-1}$ represents the reference pressure. The term Q_1/C_P denotes the nonadiabatic heating or cooling rate per unit mass of air, normalized by its specific heat capacity. The terms $U(\partial\theta/\partial x)$ and $V(\partial\theta/\partial y)$ represent zonal and meridional horizontal advection, respectively, describing heat transport caused by horizontal wind fields. The term $\omega(\partial\theta/\partial p)$ refers to the vertical advection of potential temperature, indicating changes in potential temperature driven by vertical air movements, such as ascent or descent.

In section 5, we present the thermodynamic budget analysis with the PMM-related reanalysis data to understand the physical mechanism contributing to near-surface temperature due to PMM variation.

3) LBM

The linear baroclinic model (LBM), developed from the dynamical core of the CCSR/National Institute for Environmental

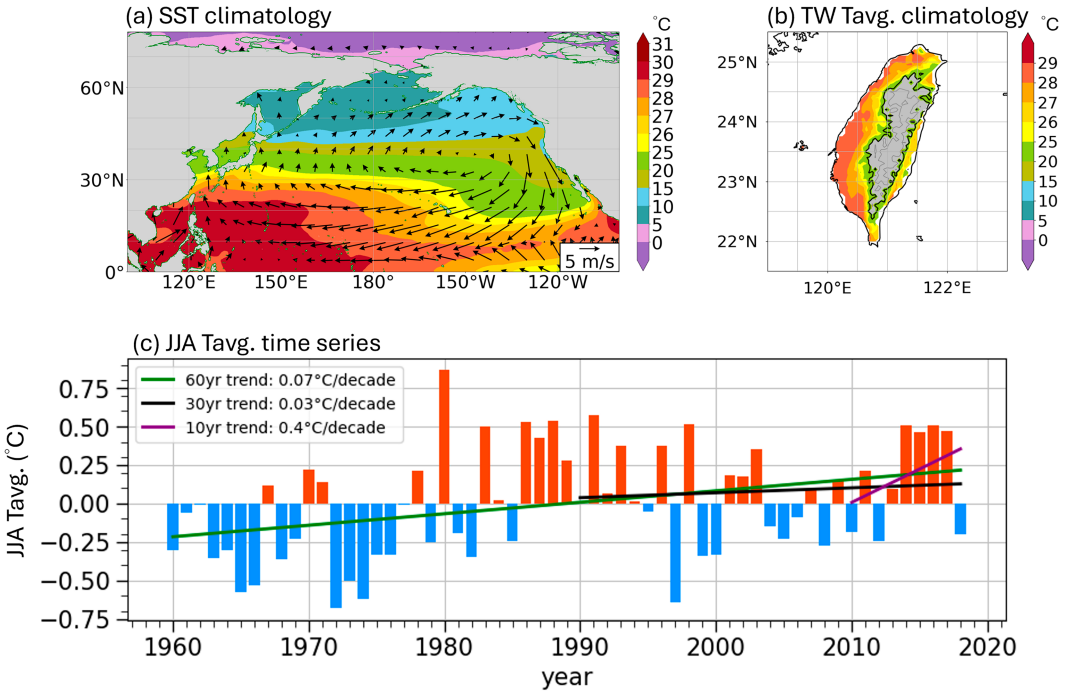

FIG. 1. Climatological analysis of the SST in the northern Pacific region and summer temperature in Taiwan. (a) Climatological SST and 850-hPa wind in JJA over the northern Pacific region. SST is based on the monthly HadISST dataset (shading; °C), and the wind is based on ERA5 reanalysis data (vector; uv, m s^{-1}). (b) Summer temperature in Taiwan, based on TCCIP gridded observational data from 1960 to 2018 (°C). The gray shading shows the region higher than the altitude of 1000 m, corresponding to the Central Mountain Range. (c) Time series of Taiwan's summer average temperature from 1960 to 2018. The green line represents the 60-yr linear trend (1960–2018), the black line represents the 30-yr linear trend (1990–2018), and the purple line represents the 10-yr linear trend (2009–18; °C).

Study (NIES) atmospheric general circulation models (AGCMs) by the University of Tokyo and the National Institute for Environmental Studies (LBM website: https://ccsr.aori.u-tokyo.ac.jp/~lbm/sub/lbm_1.html), is a simplified tool designed to study large-scale atmospheric circulation (Watanabe and Kimoto 2000, 2001; Watanabe and Jin 2003). LBM operates by linearizing the primitive equations around a prescribed basic state, removing the complexity of nonlinear interactions found in GCMs. This linear framework makes it easier to analyze atmospheric responses and feedback mechanisms. The model employs a spectral representation of the equations with a vertical sigma coordinate system and supports both multilevel baroclinic processes and single-layer barotropic models. Its dynamical core is specifically designed to compute steady-state responses to prescribed forcings and other linear dynamical scenarios, making it an effective tool for analyzing atmospheric responses and feedback mechanisms. In this study, we applied LBM to validate the relationship between PMM-like SST anomalies and the resulting large-scale circulation patterns over the North Pacific. By isolating linear responses, LBM provided clear insights into how PMM-like SST anomalies influence atmospheric dynamics, complementing the results obtained from more complex GCMs.

3. Linking decadal variation of Taiwan's summer temperature with PMM in observations

a. Decadal variation of Taiwan's summer temperature and PMM

During boreal summer, the SST over the warm pool reaches up to 30°C and expands to 20°N over the tropical western Pacific (Fig. 1a). Accompanied by a strong south–north and west–east SST gradient, a basin-scale cyclonic circulation with a center over 150°W lies over the entire northern Pacific (Fig. 1a). In the East Asia region, where Taiwan is located, strong southwesterly winds prevail, bringing in moisture from warm pool to midlatitude region, as part of the Asia monsoon circulations. At this time, the island-wide temperature can reach more than 25°C with the western plain having a maximum temperature of up to 28°C, exhibiting pronounced regional characteristics (Fig. 1b). When examining the time series of island-wide JJA-averaged summer temperatures during 1960–2018, a linear warming trend of 0.07°C per decade over the past 60 years, 0.03°C per decade over the past 30 years, and 0.4°C per decade over the past 10 years is observed (Fig. 1c). Moreover, strong decadal fluctuations are also revealed from the time series in addition to the significant warming trend, which is the focus of this study.

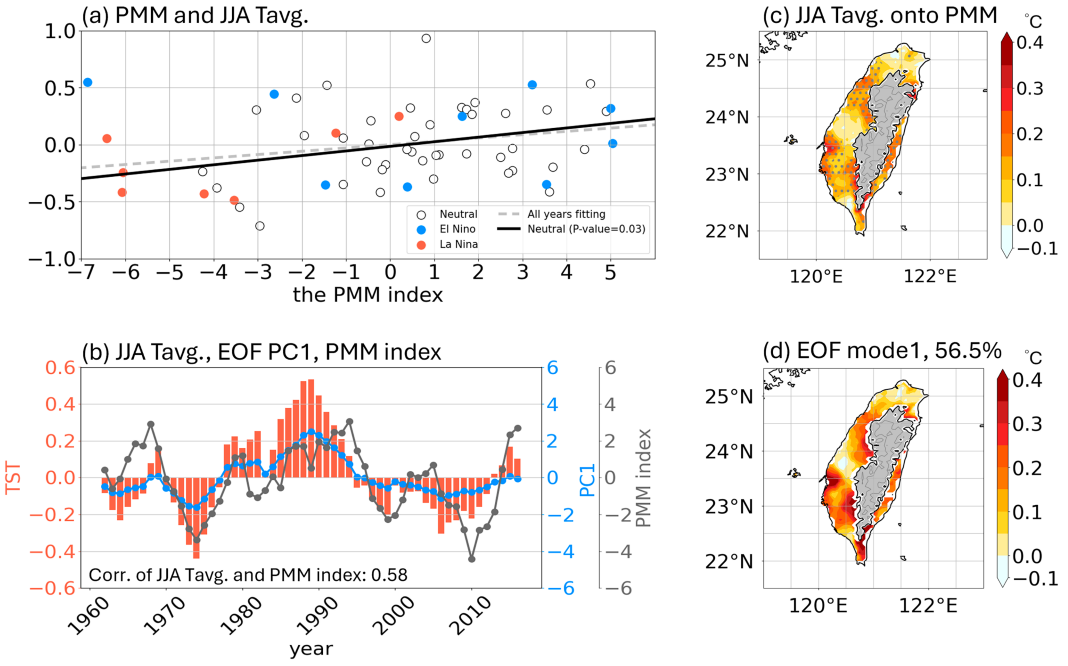

FIG. 2. Relationship between PMM and Taiwan's summer temperature. (a) Scatterplot of the JJA PMM index and Taiwan's summer temperature between 1960 and 2018 (°C). The blue circles are El Niño years, the red circles are La Niña years, and the black-bordered hollow circles are neutral years. The fitting line of neutral years is represented by the black solid line, and the fitting line of all years is represented by the gray dashed line. (b) The yearly time series of the EOF PC1 of Taiwan's summer temperature (blue line), the standardized PMM index (black line), and Taiwan's summer temperature (red bars; °C). (c) Regression map of Taiwan's summer temperature (°C) onto the standardized PMM index. The dots indicate significance at the 0.1 level. (d) The EOF mode 1 of Taiwan's summer temperature (°C).

To better consolidate the relationship between Taiwan's summer temperature and PMM from 1960 to 2018, we presented the relationship between the PMM index and the anomalies in summer temperatures in Taiwan through a scatterplot (Fig. 2a). It is clearly seen that a weak positive correlation exists between the JJA-averaged temperature and the PMM. To show the impacts of ENSO, we marked the different ENSO phases with different colors based on the Oceanic Niño index (ONI) to untangle the impacts of ENSO. Here, years with ONI values greater than 1 and less than −1 are defined as strong El Niño and La Niña years. To clarify the ENSO's influence on Taiwan's summer temperatures, we selected the year of the next summer as the strong ENSO year if the ONI exceeded the threshold in the preceding autumn or winter. For example, the ONI exceeded 1 in October 1965, and we selected the following year, 1966, as the strong ENSO year rather than 1965. As a result, we identified strong El Niño years as 1966, 1973, 1983, 1988, 1992, 1998, 2003, 2010, and 2016 and strong La Niña years as 1974, 1976, 1989, 1999, 2001, 2008, and 2011. The remaining years are defined as neutral years.

It is noteworthy that during strong La Niña years (represented by the orange dots in Fig. 2a), negative phases of PMM are often observed, while strong El Niño years are typically associated with positive PMM phases (indicated by the blue dots in Fig. 2a). However, despite these associations, there appears to be little direct correlation between ENSO and Taiwan's summer temperatures, suggesting that PMM exerts a stronger influence on Taiwan's summer temperature. As a result, the linear regression line for neutral years (solid black line in Fig. 2a) demonstrates a more robust linear fit compared to that of all years (dashed gray line in Fig. 2a). The calculated correlation coefficient for neutral years stands at 0.28 (with a p value < 0.05). This suggests that PMM does indeed play a role in influencing Taiwan's summer temperature. However, it is worth noting that focusing on all 59 years alone is sufficient to capture the relationship between PMM and Taiwan's summer temperature.

To analyze the decadal variation in Taiwan's summer temperatures, Fig. 2b presents island-wide temperature anomalies (orange bars, excluding mountain areas) smoothed with a 5-yr moving average to remove interannual fluctuations. The primary decadal variation is represented by the first EOF mode of Taiwan's temperature, which accounts for 56.5% of the total variance. The corresponding PC1, shown as the blue line in Fig. 2b, has a strong correlation coefficient of 0.95 with Taiwan's summer temperature anomalies, effectively capturing the decadal variation. The standardized PMM index from NOAA, also smoothed with a 5-yr moving average, is shown as the black line in Fig. 2b.

A comparison between Taiwan's 5-yr smoothed summer temperature anomalies (orange bars) and the standardized PMM index (black line) reveals that the PMM underwent 3–4 distinct cycles from 1960 to 2018. These cycles include a

pronounced negative phase from 1970 to 1980 (corresponding to a cold phase in Taiwan's temperatures), a positive phase from 1985 to 1995 (corresponding to a warm phase in Taiwan's temperatures), and a downward oscillation from 2000 to 2010 (another cold phase in Taiwan's temperatures). Notably, transitions in the PMM align closely with cold and warm anomalies in Taiwan's summer temperatures during these periods. The correlation coefficient between PC1 and the PMM index is 0.61, emphasizing a significant positive relationship between the primary decadal variation in Taiwan's summer temperatures and the PMM index.

The regression map of temperature anomalies in Taiwan onto the PMM summer index and EOF1 is presented in Fig. 2c and Fig. 2d, respectively. In Fig. 2c, the PMM-regressed pattern reveals temperature increases of approximately 0.2°–0.5°C in the southwestern regions (around 22.5°–23.5°N) and the central–western plain (near 24.5°N in the western lowlands). Eastern regions around 22.5°, 23.5°, and 24.5°N also exhibit warming areas of approximately 0.2°C. A resemblance is observed between the spatial pattern of PMM-regressed temperature anomalies and the EOF1 pattern of temperature anomalies (Fig. 2d), whose pattern correlation is about 0.96 (p value < 0.01). Particularly, in coastal areas and near-inland mountains (around 22.5°–23.5°N on the west side of Taiwan), summer-averaged temperatures can increase by up to 0.4°C. Warming hotspots are also evident in the central–western plain (near 24.5°N in the west), ranging approximately between 0.2° and 0.25°C, as well as in eastern regions around 22.5°, 23.5°, and 24.5°N. All warm anomaly signals in these three regions pass the statistical significance test with 90% confidence.

b. *PMM-related large-scale features over the northern Pacific and East Asia*

Based on the correlation analysis suggesting PMM's influence on Taiwan's summer temperature, we examined large-scale environmental variations across the northern Pacific associated with rising summer temperatures in Taiwan and PMM strengthening. Figure 3 shows the regressed large-scale environments for the standardized summer-averaged temperature in Taiwan (left panels) and the standardized PMM index (right panels).

Consistent with the previous studies of PMM, Fig. 3f revealed a distinct horseshoe-shaped SST warm anomaly in the eastern Pacific with one branch lying between 10° and 30°N, extending from 120°W to 180°, and one branch lying outside of the northwest coast of North America (Chiang and Vimont 2004). This warming pattern is very similar to the SST anomaly pattern regressed to the summer temperature variation in Taiwan (Fig. 3a). Both patterns show statistically significant warming anomalies in the east Pacific over the 59-yr study period. In the meantime, they also both suggest a north–south dipole pattern over the West Pacific between Japan and Taiwan and the Philippines. The tropical warm anomaly over this Southeast Asia region can be extended into the South China Sea and Maritime Continent region (Figs. 3a,f). Such analysis suggests that PMM indeed increases the summer temperature in this region. From the regression analysis with Taiwan's summer temperature variation, we observed that a one standard deviation increase in Taiwan's summer temperature corresponds to approximately a 0.3°C SST warm anomaly over the extratropical eastern Pacific. Notably, the SST increase exceeds the regional temperature rise in Taiwan, suggesting that unresolved local responses in the reanalysis data may amplify surface temperature increases over Taiwan. This finding underscores the importance of incorporating local observational data when studying regional climate impacts, particularly when local-scale processes play a significant role.

The low-level circulations during summer in Taiwan, associated with the PMM, are shown in Figs. 3b and 3g. Accompanying the SST anomaly pattern, a cyclonic circulation develops in the lower levels over the northeastern Pacific, situated at the northwestern edge of the strongest SST anomaly. At the same time, an associated low pressure system appears over the northwest Pacific near Japan. These two low pressure systems form a wave-like structure across the North Pacific, driving northeasterly winds over the western Pacific boundary, including Japan and Taiwan. This pattern produces a compensating effect on the southwesterly mean state (Fig. 1a), thereby weakening the summer monsoon system.

At the upper-atmospheric levels (Figs. 3c,h), an opposite pattern emerges with a higher (lower) geopotential height anomaly to the south (north) of 30°N. This distinctive pattern suggests the presence of a barotropic structure, which means density (or temperature) varies only with pressure and does not change with height or horizontal position, an organized large-scale structure, which arises as a result of the influence of the PMM and PMM-like warming sea surface temperature–induced circulation. When examining the vertical circulations along the cross section between 10° and 30°N, the upward motion indicates enhanced convective activity over the eastern subtropical Pacific, reflecting the circulation response to the PMM SST anomaly. The pressure anomaly system over the northwest Pacific induces upward motion between 150°E and 180°, which then shifts westward and is accompanied by downward motion across the region from 100° to 140°E in Southeast Asia (Figs. 3d,i). It is worth noting that this downward motion near Taiwan (i.e., the triangle at 120°E) is much stronger with the PMM-related forcing rather than correlated with Taiwan's summer temperature, which is consistent with the weaker SST response associated with Taiwan's summer temperature. While the primary signal is clearly observed in the subtropical regions, this subsidence response over East Asia of the Walker circulation–like pattern is consistent with the surface warming observed there and may play a role in warmer summer over East Asia.

From the perspective of velocity potential (Figs. 3e,j), the low-level and upper-level circulations between 150°E and 120°W in the Pacific can be seen as a large-scale convergence and divergence system. Figures 3e and 3j show significant divergence anomalies at the upper level (200 hPa) over the central and eastern Pacific, with the strongest divergence centered between 150° and 120°W. This coincides with the location of the strongest SST anomalies induced by the PMM (Figs. 3a,f). This upper-level divergence covers the entire eastern and central Pacific, extending westward to around 150°E. In the Asia–Pacific region, these divergence values gradually

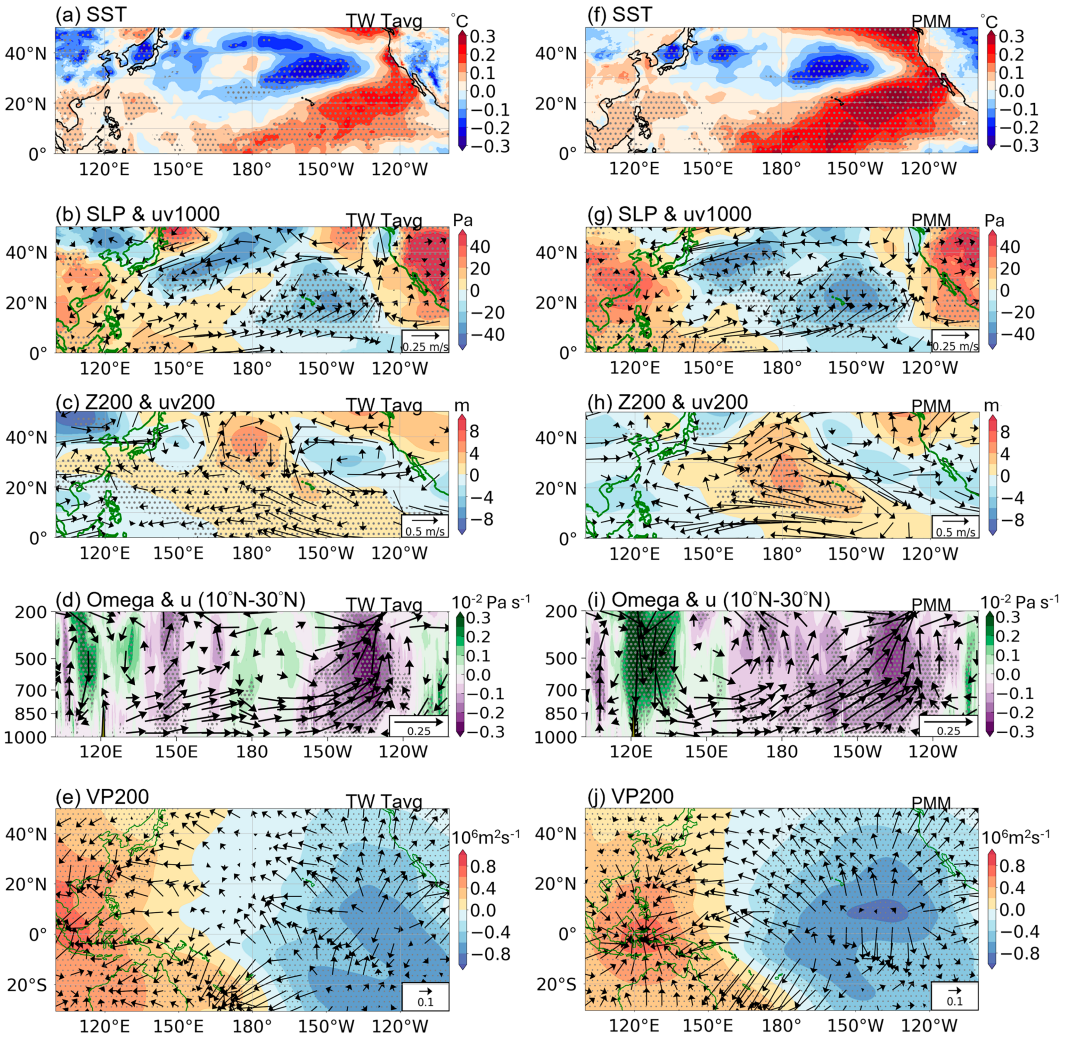

FIG. 3. Large-circulation responses in northern Pacific to variations in the standardized PMM index. (a) Regression of 2-m air temperature (shading; T2m, °C; land only) and SST (shading; °C) onto the summer mean temperature of Taiwan (derived from TCCIP observational gridded data). (b) Regression of 1000-hPa wind (vector; uv, m s^{-1}) with SLP (shading; Pa) onto the summer mean temperature of Taiwan. (c) Regression of 200-hPa wind (vector; uv, m s^{-1}) with 200-hPa geopotential height (shading; z, m) onto the summer mean temperature of Taiwan. (d) Regression of vertical wind (vectors; u, m s^{-1}; ω, 10^{-2} Pa s^{-1}) with ω (shading; 10^{-2} Pa s^{-1}) onto the summer temperature of Taiwan. (e) Regression of 200-hPa velocity potential onto the summer temperature of Taiwan. (f),(g),(h),(i),(j) As in (a), (b), (c), (d), and (e), but regressed onto the standardized PMM index. Gray dots indicate regions where the results are statistically significant at the 0.1 level. To highlight zonal variations, the zonal mean is subtracted in (b)–(d) and (g)–(i).

transition into convergence anomalies, with the strongest convergence zone appearing in the Maritime Continent region (0°, 120°E). Although Taiwan is not within the descending region of the Maritime Continent, it still experiences a significant descending zone. This is consistent with the transition between ascent and descent near 150°E in Fig. 3i and explains why a strong descending zone appears near 120°E.

We conclude that when Taiwan's summer temperatures rise, the variation in the circulation field across the North Pacific is consistent with those observed when the PMM strengthens. At the same time, the low-pressure anomalies in the lower levels of the Pacific and the high-pressure anomalies in the upper levels form a large convergence–divergence system, leading to vertical circulation systems. This results in subsidence in the Asia–Pacific region, placing Taiwan in a descending zone, which is the primary mechanism for the observed increase in summer temperatures.

c. *Local impacts of PMM over the Taiwan region via budget analysis*

1) REGIONAL FEATURES AND BUDGET ANALYSIS

To investigate the impacts of PMM circulation anomalies on East Asia and Taiwan, we focused on the regional characteristics

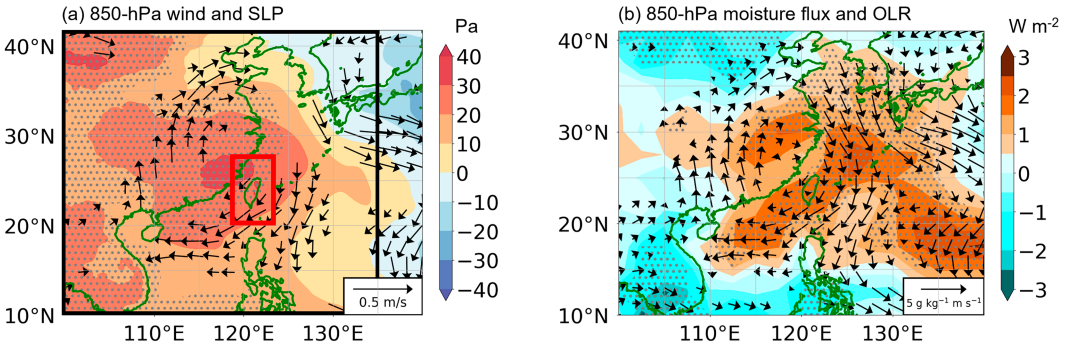

FIG. 4. Regional circulation in East Asia responses to variations in the standardized PMM index. Regression of (a) 850-hPa wind (vector; uv, m s^{-1}) and SLP (shading; Pa) and (b) moisture flux (vector; g kg^{-1} m s^{-1}) and OLR (shading; W m^{-2}) onto the standardized PMM index. The dots indicate significance at the 0.1 level. To highlight zonal variations, the zonal mean is subtracted in (a) and (b).

of PMM-related responses and analyzed the near-surface thermodynamic budget over East Asia and the surface energy budget over Taiwan.

Figure 4a shows the regional features of the SLP anomaly and 850-hPa winds of Southeast Asia centering on Taiwan. It is clearly seen that high SLP anomalies cover the East Asia region and around Taiwan between 110°E–130°W and 15°–40°N during the strengthening of the PMM (Fig. 4a). The center of the high-pressure anomalies is located at southern China coasts, very close to the northwestern part of the Taiwan Island (Fig. 4a). Along with the high-pressure anomaly, anticyclonic circulation is observed bringing in northeasterly wind anomalies over the Taiwan region (Fig. 4b). Figure 4b shows the regressed outgoing longwave radiation (OLR) anomaly and moisture fluxes at the 850-hPa level. Accompanied by the high SLP anomaly, a positive OLR anomaly prevails along the East Sea, Taiwan, and northern South China Sea at 10°–30°N and 110°–135°E, suggesting a decrease in deep convection activities over these regions. These wind anomalies counteracted the prevailing southwesterly mean winds during the summer, leading to a reduction in moisture influx from the equatorial region. This implies a less favorable environment for rainfall occurrence, contributing to drier conditions over Taiwan.

2) NEAR-SURFACE THERMODYNAMIC BUDGET

To unravel the mechanisms driving near-surface warming, we conducted a thermodynamic budget analysis using regressed fields from the ERA5 reanalysis dataset. In Figs. 5a and 5b, we present area-averaged results for two regions: East Asia (100°–135°E, 10°–40°N; the black box in Fig. 4) and Taiwan (119°–123°E, 21°–26°N; the red box in Fig. 4), respectively. These results encompass five key components of the thermodynamic equations at the 925-hPa level, as detailed in our methodology. These components encompass temporal changes in potential temperature $\partial\theta/\partial t$, the diabatic heating term Q1, zonal and meridional horizontal advection terms $p^*U(\partial\theta/\partial x)$ and $p^*V(\partial\theta/\partial y)$, and the vertical advection term $p^*\omega(\partial\theta/\partial p)$.

Over long-term averages spanning the entire summer season, we observe that temperature changes approach equilibrium, resulting in minimal variations in potential temperature $\partial\theta/\partial t$ (Figs. 5a,b). In the East Asia region, both zonal heat advection and meridional heat advection $p^*U(\partial\theta/\partial x)$ and $p^*V(\partial\theta/\partial y)$ play roles in warming, consistent with the northeasterly wind anomaly associated with the anticyclone seen in Fig. 4. Vertical advective warming $p^*\omega(\partial\theta/\partial p)$, which refers to the temperature increase caused by the vertical downward movement of air (subsidence) in an adiabatic process, primarily results from subsidence processes in this region. The diabatic cooling term Q1 is offset by the sum of all three advection terms, with magnitudes on the order of 0.01 K day^{-1}. The Q1 terms account for factors such as longwave radiation loss, evaporative cooling, and heat/cooling due to boundary layer processes.

On the other hand, when focusing on the vicinity of Taiwan's land area (Fig. 5b), we observe that the dominant warming factor is the vertical heat advection term $p^*\omega(\partial\theta/\partial p)$ with a magnitude of 0.05 K day^{-1}. The zonal advection term $p^*V(\partial\theta/\partial y)$ plays the second role of introducing warm air into the region. Similar to the East Asia region, the contribution of these two terms is balanced by the diabatic cooling term Q1, with incremental contributions from the zonal advection term $p^*\omega(\partial\theta/\partial p)$. Notably, the warming observed in the Taiwan region is approximately five times more pronounced than that observed across the entire subsidence region of East Asia.

We extended our investigation to analyze the vertical profiles of the vertical advection term and Q1, as illustrated in Figs. 5c and 5d. In Fig. 5c, we observe a vertical adiabatic warming anomaly within the region spanning 119°–123°E, particularly prominent in the middle levels between 600 and 300 hPa, with peak values exceeding 1.5 W m^{-2}. Conversely, Fig. 5d depicts a similar negative anomaly pattern in Q1 within the same region of 119°–123°E, primarily concentrated between 800 and 200 hPa. The resemblance in the patterns of positive adiabatic warming term anomalies and positive vertical adiabatic term anomalies suggests that the predominant factor contributing to temperature increases in

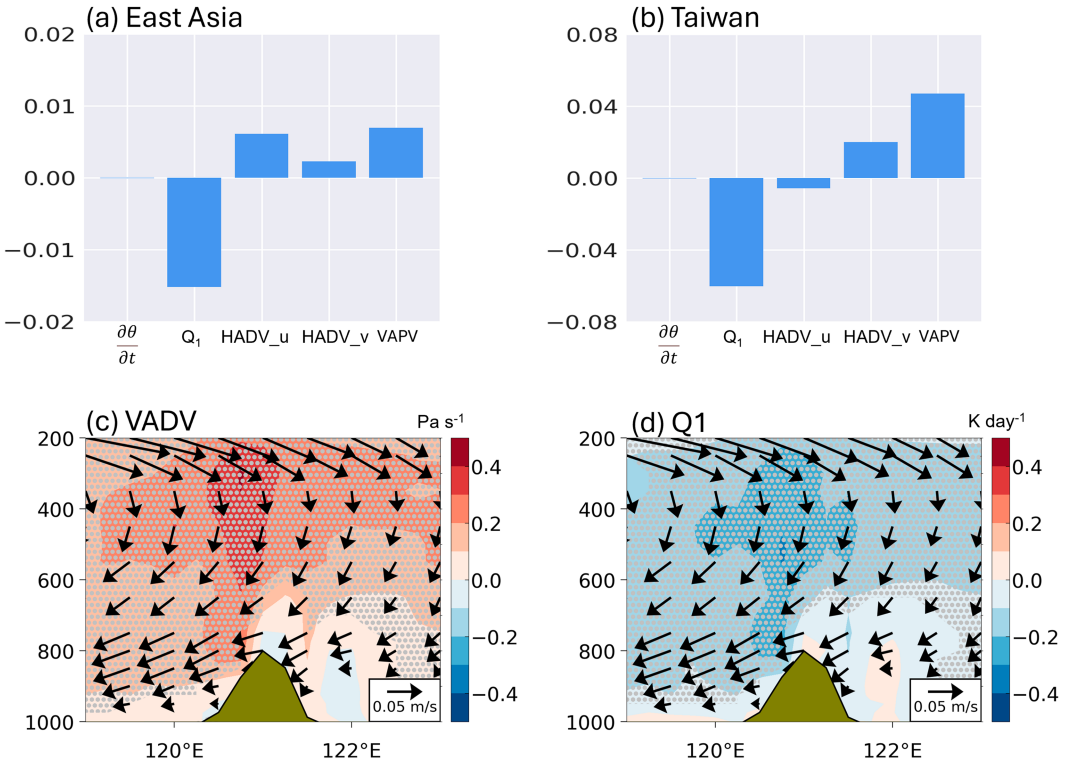

FIG. 5. Thermodynamic budget over East Asia and Taiwan. (a) Average terms of the thermodynamic budget within the black box in Fig. 4a (925 hPa; 100°–135°E, 10°–40°N). (b) As in (a), but for the area within the red box in Fig. 4a (119°–123°E, 21°–26°N). The terms include the temporal change in potential temperature $\partial\theta/\partial t$, diabatic heating Q1, zonal and meridional horizontal advection Hadv_u and Hadv_v, and the adiabatic term Vapv. All terms are expressed in units of kelvin per day. (c) Longitude–height cross sections (averaged over 21°–26°N) showing the regressed diabatic heating term (shading; K day^{-1}) along with vertical wind components (vectors; u, m s^{-1}; ω, 10^{-2} Pa s^{-1}) onto standardized PMM index. (d) As in (c), but for the Q1 term (shading; K day^{-1}) regressed onto the standardized PMM index.

this area is likely the vertical adiabatic term. Additionally, nonadiabatic energy dissipation further aids in maintaining local temperature equilibrium.

3) SURFACE ENERGY BUDGET

To further understand the surface temperature increase in Taiwan, we conducted a surface energy balance analysis within the land area of Taiwan. The formula is as follows:

$$F_S = \text{SSR} + \text{STR} + \text{SHF} + \text{LHF} + G,$$

where SSR and STR represent the net surface solar (shortwave) radiation and surface thermal (longwave) radiation, while SHF and LHF represent the sensible heat flux and latent heat flux. The ground heat flux G is generally very small, so it is not discussed in this study. All fluxes mentioned here are positive upward.

Figure 6 presents maps of all four surface flux terms in the surface energy budget regressed onto a standardized PMM index. It is evident that incoming solar radiation (SSR) increases across the entire island (Fig. 6a), with greater radiation observed in the southwestern part of Taiwan. Conversely, STR, LHF, and SHF exhibit complementary patterns, with LHF maximizing near the central mountain region and SHF peaking along the coastal areas. An island-wide average analysis reveals that among all four surface flux terms, SSR contributes approximately 0.7 W m^{-2} s^{-1} to the surface energy budget, and this is balanced by the other three terms. Specifically, we observe a decrease of approximately 1.25 W m^{-2} s^{-1} in LHF, a decrease of around 0.6 W m^{-2} s^{-1} in STR, and a decrease of about 0.1 W m^{-2} s^{-1} in SHF (Fig. 6b).

This analysis suggests that during a positive phase of the PMM, more shortwave radiation from the sun reaches the ground, leading to an increase in surface temperatures. Simultaneously, increased evaporation results in greater upward LHF, STR, and SHF, which collectively contribute to cooling the surface.

4. Assessing large-scale response to PMM-related SST anomaly in climate models

a. *LBM experiments*

In this study, we used the LBM to investigate the relationship between the PMM and the North Pacific circulation. LBM simplifies atmospheric dynamics by linearizing the governing equations, focusing specifically on the forced response to the

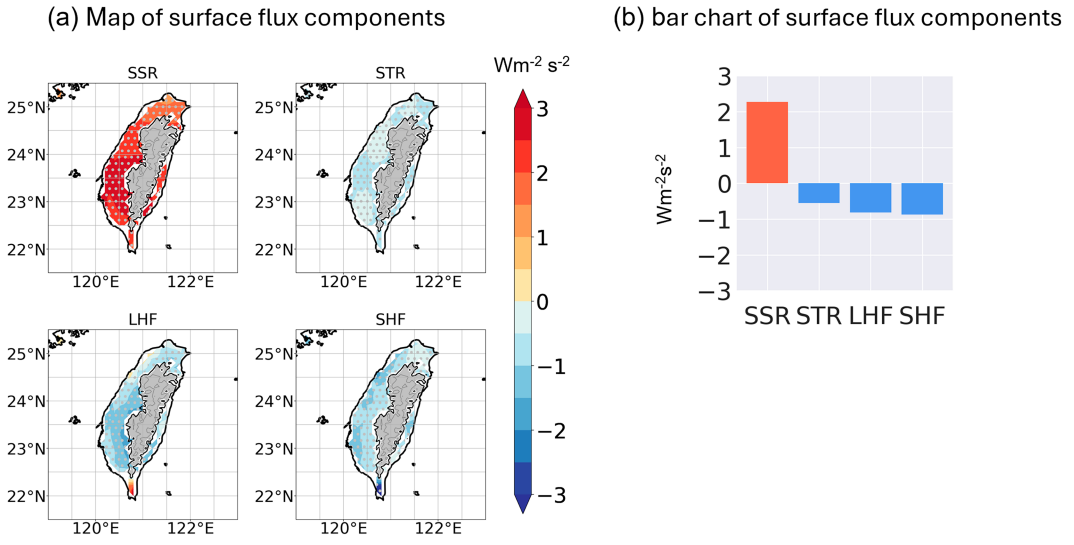

FIG. 6. Surface energy budget terms over Taiwan regressed with the PMM index based on ERA5 reanalysis. (a) Each term of surface heat budget, including SSR, STR, LHF, and SHF (W m^{-2} s^{-2}). (b) Regional average of surface heat budget in Taiwan with average over 119°–123°E, 21°–26°N (W m^{-2} s^{-2}).

PMM while eliminating interference from nonlinear processes. Compared to more complex nonlinear models (e.g., AGCMs), LBM features a simplified framework, making its results easier to interpret. Additionally, LBM quantifies the direct impact of PMM on the structure of the North Pacific circulation and effectively distinguishes PMM from other climate modes (e.g., ENSO), providing a valuable diagnostic tool for understanding how PMM affects regional climate changes. In the experiment, we introduced a heating force representing the PMM pattern, as shown by the red contour lines in Fig. 7a. This heat source produced divergent ascending motion in the upper levels over the eastern Pacific, while convergent subsiding motion dominates the upper levels of the western Pacific, covering regions such as Taiwan, the Philippines, and the Maritime Continent (Fig. 7a). Figure 7b further reveals the lower-atmospheric circulation features corresponding to the ascending region in the eastern Pacific and the subsiding region in the western Pacific shown in Fig. 7a. A significant low-pressure anomaly emerges in the central to eastern Pacific (150°E–120°W), while a high-pressure anomaly forms in the western Pacific, centered along the southern coast of China, near the Taiwan landmass. Taiwan is influenced by the high-pressure subsidence zone, dominated by anticyclonic circulation. This likely weakens the prevailing southwesterly monsoon during summer, reducing the inflow of moist air from the south, leading to drier conditions in Taiwan and facilitating sustained high temperatures. Figure 7c further illustrates the upper-atmospheric response, with a high-pressure anomaly in the upper levels of the eastern Pacific corresponding to a low-pressure anomaly in the lower levels. Overall, the LBM experiment successfully reproduced the Pacific circulation response to PMM observed in data, confirming the significant influence of PMM on the North Pacific atmospheric circulation and regional climate. This demonstrates that PMM variability not only has profound impacts on the structure of the North Pacific circulation but may also influence regional climate features, such as those in Taiwan, by modulating subsidence motion.

b. *CMIP6 historical runs*

In addition to the LBM experiments, we assessed the large-scale features associated with PMM-related SST patterns simulated by climate models using historical simulations from the CMIP6 model ensemble. We employed the methodology of Richter et al. (2022) to define the PMM index, based on the principal component analysis of EOF1 of the eastern Pacific SST. Our findings indicate that 86.5% of the CMIP6 models successfully captured the PMM pattern in the first mode, with pattern correlation coefficients exceeding 0.3, and 65% of the models demonstrated correlation coefficients greater than 0.6 (p value < 0.05), thereby confirming the CMIP6 models' effectiveness in reproducing the PMM pattern (Fig. S1). Notably, the PMM pattern may appear in EOF mode 2 instead of mode 1 in some models, such as Taiwan Earth System Model, version 1 (TaiESM1) (not shown).

The ensemble mean SST pattern related to the PMM, as derived from the CMIP6 models, is presented in Fig. 8a. This pattern exhibits considerable similarities with the observed PMM-related SST pattern depicted in Fig. 3f. The subsequent panels in Fig. 8 illustrate the large-scale features associated with the PMM indices from the CMIP6 model ensemble. The regressed SLP analysis reveals a low-pressure anomaly over the North Pacific, extending approximately from 115°E to 120°W, accompanied by a high SLP anomaly over the North American and East Asian continental regions (Fig. 8b). The modeled low-pressure anomaly pattern closely resembles that observed in Fig. 3b, although it extends westward to approximately 135°E, indicating a westward shift of about 20° relative to the observations.

The zonal cross-sectional analysis over 10°–30°N in the northern Pacific reveals the strongest ascent signal around

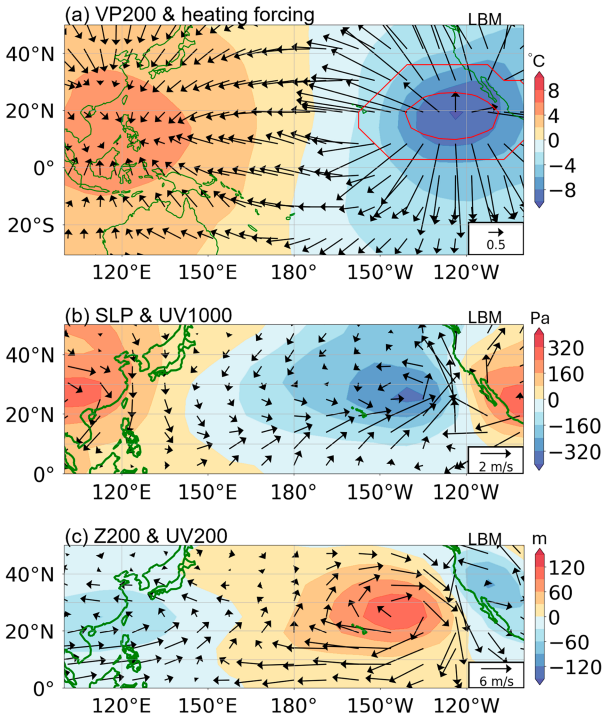

FIG. 7. PMM heating forcing and large-scale responses simulated by LBM. (a) 200-hPa velocity potential (shading; 10^6 m^2 s^{-1}) and the heating forcing in the LBM experiment (red contour line). The arrows represent the 200-hPa divergent wind field (vectors). These vectors highlight the atmospheric circulation response to the imposed heating forcing. (b) SLP (shading; Pa) and 1000-hPa wind (vectors; m s^{-1}). (c) 200-hPa geopotential height (shading; m) with 200-hPa wind (vectors; m s^{-1}). To emphasize zonal variation, the zonal mean is subtracted in all panels.

150°W, corresponding to the region just west of the PMM-related warm SST anomaly pattern, with notable upward motion extending through the troposphere (Fig. 8d). In contrast, there is significant descent in the western Pacific, particularly east of 150°E and most prominently between 110° and 120°E, where strong subsidence is observed from the surface up to about 500 hPa. Such features can be more clearly seen in velocity potential anomaly fields at 200 hPa in the North Pacific (Fig. 8e). This pattern, characterized by rising motion in the central–eastern Pacific and sinking motion in the western Pacific, reflects the large-scale atmospheric response typically associated with PMM-related SST anomalies. The subsidence and ascent responses simulated by the CMIP6 models mirror the observed patterns in Figs. 3i and 3j, with the subsidence region extending further westward into the Asia–Pacific region.

We assessed model consistency in Fig. 8 by marking regions where at least 60% of the 37 CMIP6 models exhibit the same sign, indicated by dots. The results show that the models generally agree over the east Pacific but demonstrate less consistency over the western Pacific, indicating greater uncertainty in simulating the regional impacts of PMM-related SST patterns in East Asia. This suggests that while CMIP6 models produce a robust response to the PMM SST pattern in the eastern North Pacific, they struggle to accurately simulate its teleconnections in the Asia–Pacific region. This finding indicates the need for further model development to better understand and address the sources of this uncertainty.

5. Discussion and summary

In this study, we utilized high-resolution 5-km local-scale temperature data from Taiwan to investigate the influence of the PMM on decadal variations in Taiwan's summer temperatures. Our findings suggest that the PMM serves as a significant climate modulator, exerting a pronounced influence on decadal-scale temperature patterns in Taiwan (Fig. 9). Regression analysis with global reanalysis data revealed that island-wide mean temperatures tend to increase when the PMM strengthens. This temperature rise is attributed to warm SST anomalies in the eastern Pacific associated with the PMM, which trigger a broad atmospheric response across the Pacific basin. This response includes the propagation of a wave train across the northern Pacific, resulting in a high-pressure anomaly extending from the west into the central Pacific, accompanied by subsidence and anticyclonic circulation over East Asia, including Taiwan. The resulting atmospheric stability enhances incoming surface solar radiation over Taiwan, leading to increased surface temperatures. To simulate the atmospheric response to PMM-induced SST anomalies and investigate the mechanisms driving large-scale circulation patterns, we employed LBM simulations. These simulations captured key features observed in reanalysis data, including low-pressure anomalies in the east Pacific and high-pressure anomalies over East Asia, associated with subsidence and anticyclonic circulation over Taiwan. CMIP6 historical simulations further confirmed the PMM's influence, with 86.5% of models capturing the PMM pattern in the first EOF mode. Modeled responses showed consistent low-pressure anomalies in the east Pacific and ascent–descent patterns over the Pacific, though features shifted slightly westward compared to observations. However, CMIP6 models demonstrated greater uncertainty in simulating teleconnections over East Asia, suggesting a need for improved regional simulations to capture the PMM's impacts more accurately. Additionally, an AMIP experiment conducted with TaiESM1 captured only limited features of the PMM-induced circulation in the North Pacific (Fig. S1). While the CMIP6 ensemble provides robust large-scale responses to PMM patterns that are generally consistent with observations, many CMIP6 models still face challenges in accurately simulating these responses (not shown). The limited response in TaiESM1 experiments exemplifies this issue. Previous analysis of TaiESM1 historical runs reveals significant biases in SST variability over the east Pacific, not only in the mean state but also in the ENSO response (Wang et al. 2021; Y.-C. Wang et al. 2023). These biases likely stem from deficiencies in SST–cloud–circulation interactions in this region which may hinder TaiESM1's ability to simulate climate variability associated with the PMM. When compared with LBM simulations, CMIP6 models show less consensus in the subsidence region induced by PMM SST patterns over East Asia. This suggests that additional processes included in Earth system models

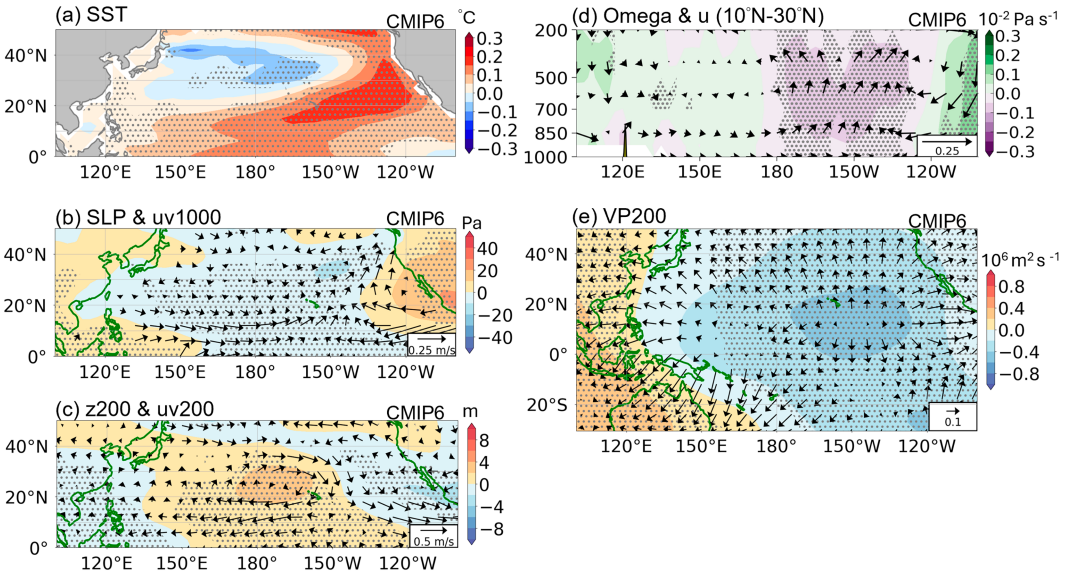

FIG. 8. SST patterns and large-scale features associated with PMM modes derived from CMIP6 historical simulations. Regression of (a) SST (shading; °C), (b) 1000-hPa wind (vector; uv, m s^{-1}) with SLP (shading; Pa), (c) 200-hPa wind (uv, m s^{-1}) with 200-hPa geopotential height (shading; z, m), (d) vertical wind (vectors; u, m s^{-1}; ω, 10–2 Pa s^{-1}) with ω (shading; Pa s^{-1}), (e) 200-hPa velocity potential onto the PC1 of the eastern Pacific SST from CMIP6, representing standardized PMM index. Gray dots indicate grid points where more than 60% of the models simulate values with the same sign as the observational data. To emphasize zonal variation, the zonal mean is subtracted in (b)–(d).

might introduce uncertainties that affect teleconnection patterns. Our findings highlight the need for further research to understand how these biases in CMIP6 models affect the robustness of PMM-related large-scale circulation patterns over the Pacific. These limitations underscore the heightened sensitivity of this region to PMM impacts, which are strongly influenced by unique atmospheric structures, geographical features, and regional nonlinear processes over Taiwan and East Asia. Future research and simulations must incorporate refined regional physical processes and geographic characteristics to improve our understanding and prediction of PMM impacts.

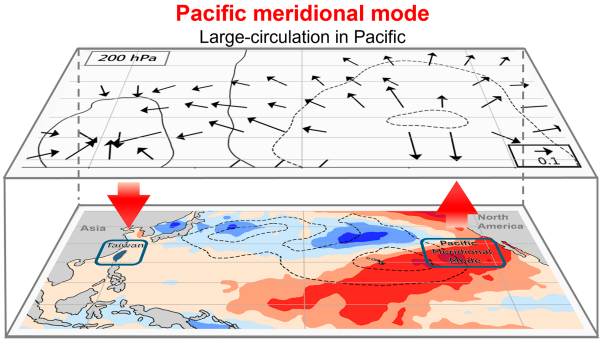

FIG. 9. The diagram illustrates the physical process through which the PMM increases summer temperatures in Taiwan. In the lower layer, shading represents SSTA regressed onto the standardized PMM index, consistent with the SSTA in Fig. 3f. The black contour lines indicate SLP regressed onto the same index, with dashed-line values of −30 and −50, corresponding to the SLP shown in Fig. 3g. In the upper layer, contour lines represent the 200-hPa velocity potential regressed onto the standardized PMM index, with values of 0.8, 0.4, 0, −0.4, and −0.8, while black vectors indicate the directions of convergence and divergence, as shown in Fig. 3j. Red vectors between the lower and upper layers illustrate the circulation anomalies driven by the wave train associated with PMM-related SSTA.

Regionally, the local features of topography and land–sea interactions in Taiwan significantly influence the temperature patterns associated with PMM-induced large-scale circulations, as shown in Figs. 3c and 3d. The Central Mountain Range, located in central Taiwan, plays a particularly important role. Our analysis indicates that temperature anomalies are most pronounced around the foothills of the Central Mountain Range, on both its western and eastern sides. This suggests that even medium-altitude regions are susceptible to warming when large-scale subsidence prevails. This is likely due to subsidence-induced reductions in cloud cover, which create a drier environment that limits surface evaporation, making these areas more vulnerable to temperature increases. Furthermore, the low-level anticyclonic flow anomalies associated with the PMM pattern weaken moisture transport from the southwesterly monsoonal flow. This suppression of moisture transport enhances downslope motions on the leeward side of the Central Mountain Range, leading to strong adiabatic warming that further elevates surface temperatures, resulting in localized hotspots, particularly over the western plains of Taiwan. Similar lee-side subsidence effects have been noted in previous studies (e.g., Wu et al. 2020). These interactions highlight the critical role of Taiwan's unique geographic and topographic features in shaping local climate responses to PMM-induced large-scale circulations.

Remotely, Taiwan's summer climate is shaped by interactions between the PMM and other regional factors. During

positive PMM phases, the WNP subtropical high (WNPSH) strengthens and extends westward, inducing subsidence and suppressing southwesterly monsoonal moisture transport, which prolongs heatwave conditions. While typhoons can cause extreme heat through Foehn effects as they cross the Central Mountain Range, studies suggest their frequency decreases during positive PMM phases, potentially reducing typhoon-driven heat events but increasing the occurrence of general hot days. Additionally, long-term oceanic patterns such as PDO and ENSO may modulate PMM's impacts. These interactions highlight the need for further research to improve understanding of PMM's decadal influence on Taiwan's climate.

In summary, we build upon prior research highlighting the PMM's role in reducing typhoon frequency across East Asia and its potential to lead to drought conditions in Taiwan (Hung and Shih 2019). We extend this understanding by suggesting that positive PMM phases are likely to bring hot and dry summer conditions. This consecutive occurrence of dry winters followed by warm summers increases the risk of compound effects, which in turn strains agriculture and electricity supply during the summer months. Importantly, our analysis identifies regional variations in PMM-related warming across Taiwan, notably in the southwest, southeast, and central–west regions. These differences result from interactions between PMM-induced circulation anomalies and local atmospheric patterns influenced by the central mountains. Our study emphasizes the need for refined modeling efforts to identify regions prone to severe climate hazards, providing valuable insights for effective local adaptation strategies.

In a broader context, Taiwan has experienced a rise in average temperatures of approximately 1.3°C over the past century during 1900–2012 (Hsu et al. 2017) and an accelerating trend of warming observed in the past 50 and 10 years. This warming trend poses significant risks to ecosystems, the economy, and public health and safety. Our study further suggests that variations in PMM may also exert substantial influences on Taiwan's summer temperatures, with an estimated impact of around 0.1°C for every one standard deviation change in the PMM index. Over the past six decades (1960–2018), there have been 4–5 cycles of PMM transitions, with amplitudes of the PMM index reaching up to two standard deviations, resulting in a temperature increase of 0.2°C during the positive phase of PMM. The adaptation to such warm phases driven by PMM variations may be as significant as the ongoing global warming trend in the coming decades. Additionally, research has indicated that global warming has intensified the wind–evaporation–sea SST thermodynamic feedback, further complicating the future regional impacts of PMM (Liguori and Di Lorenzo 2018). Continued research efforts will be pivotal in enhancing our understanding of the relative impacts of PMM and global warming on Taiwan's summer temperatures and the broader regional climate in East Asia.

Acknowledgments. We thank Professor Huang-Hsiung Hsu for insightful suggestions and feedbacks of this study. This work was supported by the National Science and Technology Council under Grants MOST 113-2111-M-002-016, 113-2111-M-003-005, 113-2111-M-001-009, and 112-2923-M-001-003-MY4. Additional funding was supported by the Industrial Technology Research Institute in Taiwan of the project "Collection of offshore meteorological observation, satellite, and reanalysis data in Taiwan and the Asia–Pacific region." We are grateful to the Taiwan Climate Change Projection Information and Adaptation Knowledge Platform (TCCIP) for providing the data. We are also grateful to the National Center for High-Performance Computing of Taiwan for providing the facilities for the computational procedures.

Data availability statement. ERA5 and ERA5-Land datasets are available at https://www.ecmwf.int/en/forecasts/datasets/reanalysis-datasets/era5; ERSST is available at https://www.ncei.noaa.gov/products/extended-reconstructed-sst; the 5 km × 5 km high-resolution horizontal grid data of Taiwan were provided by Taiwan Climate Change Projection Information and Adaptation Knowledge Platform (TCCIP) at https://tccip.ncdr.nat.gov.tw/TCCIP.

REFERENCES

Chen, J.-M., F.-C. Lu, and C.-F. Shih, 2008: Decadal oscillation of fall temperature in Taiwan. *Terr. Atmos. Oceanic Sci.*, **19**, 497–504, https://doi.org/10.3319/TAO.2008.19.5.497(A).

Chiang, J. C. H., and D. J. Vimont, 2004: Analogous Pacific and Atlantic meridional modes of tropical atmosphere–ocean variability. *J. Climate*, **17**, 4143–4158, https://doi.org/10.1175/JCLI4953.1.

Dunstone, N., and Coauthors, 2022: Towards useful decadal climate services. *Bull. Amer. Meteor. Soc.*, **103**, E1705–E1719, https://doi.org/10.1175/BAMS-D-21-0190.1.

Gao, S., L. Zhu, W. Zhang, and Z. Chen, 2018: Strong modulation of the Pacific meridional mode on the occurrence of intense tropical cyclones over the western North Pacific. *J. Climate*, **31**, 7739–7749, https://doi.org/10.1175/JCLI-D-17-0833.1.

Goddard, L., 2016: From science to service. *Science*, **353**, 1366–1367, https://doi.org/10.1126/science.aag3087.

Henny, L., C. D. Thorncroft, H.-H. Hsu, and L. F. Bosart, 2021: Extreme rainfall in Taiwan: Seasonal statistics and trends. *J. Climate*, **34**, 4711–4731, https://doi.org/10.1175/JCLI-D-20-0999.1.

——, ——, ——, and ——, 2023: Changes in extreme precipitation in Taiwan's Mei-yu season. *Quart. J. Roy. Meteor. Soc.*, **149**, 1810–1832, https://doi.org/10.1002/qj.4483.

Hersbach, H., and Coauthors, 2020: The ERA5 global reanalysis. *Quart. J. Roy. Meteor. Soc.*, **146**, 1999–2049, https://doi.org/10.1002/qj.3803.

Hong, C.-C., M.-Y. Lee, H.-H. Hsu, and W.-L. Tseng, 2018: Distinct influences of the ENSO-like and PMM-like SST anomalies on the mean TC genesis location in the western North Pacific: The 2015 summer as an extreme example. *J. Climate*, **31**, 3049–3059, https://doi.org/10.1175/JCLI-D-17-0504.1.

Hoskins, B., 2013: The potential for skill across the range of the seamless weather-climate prediction problem: A stimulus for our science. *Quart. J. Roy. Meteor. Soc.*, **139**, 573–584, https://doi.org/10.1002/qj.1991.

Hsu, H.-H., and Coauthors, 2017: Climate Change in Taiwan: Scientific Report 2017. Tech. Rep., 666 pp.

Huang, W.-R., and Y.-H. Chang, 2018: Characteristics and mechanisms of the diurnal variation of winter precipitation in Taiwan. *Int. J. Climatol.*, **38**, 3058–3068, https://doi.org/10.1002/joc.5482.

Hung, C.-w., and M.-F. Shih, 2019: Analysis of severe droughts in Taiwan and its related atmospheric and oceanic environments. *Atmosphere*, **10**, 159, https://doi.org/10.3390/atmos10030159.

Kao, P.-k., C.-w. Hung, and C.-C. Hong, 2018: Increasing influence of central Pacific El Niño on the inter-decadal variation of spring rainfall in northern Taiwan and southern China since 1980. *Atmos. Sci. Lett.*, **19**, e864, https://doi.org/10.1002/asl.864.

——, C.-C. Hong, A.-Y. Huang, and C.-C. Chang, 2022: Intensification of interannual cross-basin SST interaction between the North Atlantic tripole and Pacific meridional mode since the 1990s. *J. Climate*, **35**, 5967–5979, https://doi.org/10.1175/JCLI-D-21-0594.1.

Liguori, G., and E. Di Lorenzo, 2018: Meridional modes and increasing Pacific decadal variability under anthropogenic forcing. *Geophys. Res. Lett.*, **45**, 983–991, https://doi.org/10.1002/2017GL076548.

Lo, T.-T., and H.-H. Hsu, 2008: The early 1950s regime shift in temperature in Taiwan and East Asia. *Climate Dyn.*, **31**, 449–461, https://doi.org/10.1007/s00382-007-0311-4.

Luo, M., N.-C. Lau, W. Zhang, Q. Zhang, and Z. Liu, 2020: Summer high temperature extremes over China linked to the Pacific meridional mode. *J. Climate*, **33**, 5905–5917, https://doi.org/10.1175/JCLI-D-19-0425.1.

Rayner, N. A., D. E. Parker, E. B. Horton, C. K. Folland, L. V. Alexander, D. P. Rowell, E. C. Kent, and A. Kaplan, 2003: Global analyses of sea surface temperature, sea ice, and night marine air temperature since the late nineteenth century. *J. Geophys. Res.*, **108**, 4407, https://doi.org/10.1029/2002JD002670.

Richter, I., M. F. Stuecker, N. Takahashi, and N. Schneider, 2022: Disentangling the North Pacific Meridional Mode from tropical Pacific variability. *npj Climate Atmos. Sci.*, **5**, 94, https://doi.org/10.1038/s41612-022-00317-8.

Ruti, P. M., and Coauthors, 2020: Advancing research for seamless Earth system prediction. *Bull. Amer. Meteor. Soc.*, **101**, E23–E35, https://doi.org/10.1175/BAMS-D-17-0302.1.

Song, J., P. J. Klotzbach, Y.-F. Wang, and Y. Duan, 2023: Asymmetric influence of the Pacific meridional mode on tropical cyclone formation over the western North Pacific. *Int. J. Climatol.*, **43**, 6578–6589, https://doi.org/10.1002/joc.8220.

Trenberth, K. E., M. Marquis, and S. Zebiak, 2016: The vital need for a climate information system. *Nat. Climate Change*, **6**, 1057–1059, https://doi.org/10.1038/nclimate3170.

Tseng, W.-L., S.-Y. Lin, Y.-C. Wang, S.-H. Lo, M.-H. Lo, S.-Y. Lee, C.-T. Tsai, and H.-H. Hsu, 2023: Impact of Pacific–Japan pattern on temperature and heatwave events in summer over Taiwan. *Int. J. Climatol.*, **43**, 7067–7081, https://doi.org/10.1002/joc.8252.

Wang, C., F. Meiling, B. Wang, L. Wu, and J.-J. Luo, 2023: Pacific decadal oscillation modulates the relationship between Pacific Meridional Mode and tropical cyclone genesis in the western North Pacific. *Geophys. Res. Lett.*, **50**, e2022GL101710, https://doi.org/10.1029/2022GL101710.

Wang, Y.-C., and Coauthors, 2021: Performance of the Taiwan Earth System Model in simulating climate variability compared with observations and CMIP6 model simulations. *J. Adv. Model. Earth Syst.*, **13**, e2020MS002353, https://doi.org/10.1029/2020MS002353.

——, W.-L. Tseng, Y.-L. Chen, S.-Y. Lee, H.-H. Hsu, and H.-C. Liang, 2023: ENSO statistics, teleconnections, and atmosphere–ocean coupling in the Taiwan Earth System Model version 1. *Geosci. Model Dev.*, **16**, 4599–4616, https://doi.org/10.5194/gmd-16-4599-2023.

Watanabe, M., and M. Kimoto, 2000: Atmosphere-ocean thermal coupling in the North Atlantic: A positive feedback. *Quart. J. Roy. Meteor. Soc.*, **126**, 3343–3369, https://doi.org/10.1002/qj.49712657017.

——, and ——, 2001: Corrigendum. *Quart. J. Roy. Meteor. Soc.*, **127**, 733–734, https://doi.org/10.1002/qj.49712757223.

——, and F.-F. Jin, 2003: A moist linear baroclinic model: Coupled dynamical–convective response to El Niño. *J. Climate*, **16**, 1121–1139, https://doi.org/10.1175/1520-0442(2003)16<1121:AMLBMC>2.0.CO;2.

Wu, Y.-c., J.-L. Chu, and Y.-C. Yu, 2020: Climatology and the interannual variability of the high-temperature extremes in Taiwan. *J. Geophys. Res. Atmos.*, **125**, e2019JD030992, https://doi.org/10.1029/2019JD030992.

Yanai, M., S. Esbensen, and J.-H. Chu, 1973: Determination of bulk properties of tropical cloud clusters from large-scale heat and moisture budgets. *J. Atmos. Sci.*, **30**, 611–627, https://doi.org/10.1175/1520-0469(1973)030<0611:DOBPOT>2.0.CO;2.

Yang, C.-d., C.-Y. Wang, and S.-y. Lin, 2024: The production process of version 2 (V2) gridded observational rainfall data records (4.1.1 version). 10 pp., https://tccip.ncdr.nat.gov.tw/upload/data_profile/20220706104221.pdf.

Yu, J.-Y., 2015: Precursors of ENSO beyond the tropical Pacific. *US CLIVAR Variations*, **13**, 15–20.